Computational Geosciences (2019) 23:21–33
https://doi.org/10.1007/s10596-018-9781-1

ORIGINAL PAPER

A simple projection method for the coupled Navier-Stokes and Darcy flows

Ming-Chih Lai[1] · **Ming-Cheng Shiue**[1] · **Kian Chuan Ong**[2]

Received: 26 September 2017 / Accepted: 25 September 2018 / Published online: 1 October 2018

Abstract

The flow through both an incompressible fluid region and a porous medium occurs in a wide range of applications encompassing industrial processes and geological phenomena. Recently, the fluid transport phenomena across the interface between the distinct regions have received increasing attention both from the mathematical and the numerical points of view. The primary objective of the present study lies in the development of a simple and efficient method for the computations of coupled Navier-Stokes and Darcy flows with complex interface conditions. A finite difference projection method is developed within a staggered grid framework to solve the coupled system in a segregated manner using primitive variables. Numerical simulations are carried out to demonstrate the order of convergence and its capability. The proposed method renders the versatility in solving the coupled system, and it is readily extendible to multi-physics fluid flows and turbulent flows for a broad range of applications.

Keywords Coupled Navier-Stokes and Darcy flows · Beavers-Joseph-Saffman interface conditions · Projection method · Finite difference · Staggered grid

1 Introduction

The fluid transport phenomena across the interface between an incompressible fluid region and a porous medium are often encountered in various science and engineering applications. A plethora of physicochemical phenomena, such as surface reaction, may occur at this interface. Those coupled problems have received increasing attention both from the mathematical and the numerical points of view. The mathematical model consists of the Navier-Stokes or Stokes equations in the fluid region and the Darcy law in the porous medium. Despite the fact that the numerical schemes of each sub-problem are well-known and well-developed, the numerical analysis of the coupled problem is still interesting to investigate. Therefore, it is prudent that attention is focused on developing a highly efficient numerical method for solving the system.

The numerical algorithm is required to compute different sets of conservation laws on different regions, on top of the coupling with complex interface conditions. Over the last decade, various approaches have been developed in the literature. For instance, based on whether these different sets of variables in different regions are solved simultaneously, finite element methods can be classified into two categories: coupled finite element methods and decoupled finite element methods. Coupled finite element methods include the coupled mixed finite element methods [1–9], coupled discontinuous Galerkin (DG) methods [10–14], coupled hybrid methods [14], and coupled multi-grid methods [15]. Decoupled finite element methods include the domain decomposition methods [16–21], Lagrange multiplier methods [22–24], two-grid methods [25, 26], and partitioned time stepping methods [27, 28]. Besides finite element methods, other approaches such as boundary integral methods [29, 30], a spectral method [31], a pseudo-spectral least squares method [32], and a finite volume

✉ Kian Chuan Ong
kcong@ncts.ntu.edu.tw

Ming-Chih Lai
mclai@math.nctu.edu.tw

Ming-Cheng Shiue
mshiue@math.nctu.edu.tw

[1] Department of Applied Mathematics, National Chiao Tung University, 1001 Ta Hsueh Road, Hsinchu 300, Taiwan

[2] National Center for Theoretical Sciences, No. 1, Sec. 4, Roosevelt Road, Astronomy-Mathematics Building, National Taiwan University, Taipei 10617, Taiwan

method [33] have already been studied and recently, a finite difference method based on an immersed interface method [34] was considered (as for more sophisticated variations of Navier-Stokes/Darcy or Stokes/Darcy systems that consider two-phase flow, poroelasticity, dual porosity media and so on, we refer the interested readers to see [35–42] for more details). Comprehensive reviews of the numerical algorithms in the literature revealed that the vast majority are based on finite element method instead of other discretization practice. Furthermore, the transient solutions [43] are rarely investigated as opposed to the steady-state solutions. Contrary to Stokes and Darcy system, there are also significantly less effort invested in the development on Navier-Stokes and Darcy system [12, 26, 44–47].

The primary objective of the present study lies in the development of a simple and efficient method for the computations of coupled Navier-Stokes and Darcy flows with complex interface conditions. The proposed method is based on the projection method [48] in conjunction with appropriate interface boundary conditions. The fundamental discretization approach is the finite difference method based on the staggered grid framework. The proposed projection method solves the velocities, Darcy velocities, pressure, and scaled pressure in a segregated procedure.

The mathematical analysis of the numerical algorithm for coupling Stokes and Darcy flows based on the staggered grid framework is studied in [49]. In [49], the authors considered the steady-state solution. In the present article, nonstationary Navier-Stokes and Darcy flows based on the first-order projection method in the temporal variable and finite difference approximation in spatial variables are performed. Numerical simulations are conducted for the model problem with a designed analytical solution and applications in order to investigate the numerical accuracy and functionality of the method. The aforementioned methodology is flexible due to its segregated algorithm, and therefore it can be extended for a broad range of applications with relative ease. Numerical experiments suggest that the numerical scheme for coupling Navier-Stokes and Darcy flows has the same theoretical results as the case of only Navier-Stokes flow.

2 Governing equations

Consider a model problem consisting of an incompressible flow in the fluid region Ω_F with boundary $\partial\Omega_F$ and a Darcy flow in the porous medium Ω_D with boundary $\partial\Omega_D$. The bounded domains Ω_F and $\Omega_D \subset \mathbb{R}^2$ are separated by an interface Γ with the unit normal vector $\mathbf{n}$ pointing out of the fluid domain Ω_F. The schematic description of the model is depicted in Fig. 1. In the fluid region Ω_F, the incompressible Navier-Stokes equations for the velocity $\mathbf{u} = (u, v)$ and the pressure p can be read as

$$\frac{\partial \mathbf{u}}{\partial t} + (\mathbf{u}\cdot\nabla)\,\mathbf{u} + \nabla p = \nu\Delta\mathbf{u} + \mathbf{F}, \quad \text{in } \Omega_F, \tag{1}$$

$$\nabla\cdot\mathbf{u} = 0, \quad \text{in } \Omega_F, \qquad (\mathbf{u} \text{ is given on } \partial\Omega_F) \tag{2}$$

where ν is the kinematics viscosity and $\mathbf{F} = (f, g)$ stands for the external forcing term. On the other hand, the porous medium can be defined by a model where the fluid and solid occupy the whole region on the macroscopic scale. The porous medium is a homogeneous continuum domain where a representative volume element is larger than the average pore size but much smaller than the length scale of the system. For modeling this saturated flow in homogeneous porous media domain Ω_D, the Darcy law can be used, i.e.,

$$\mathbf{u}_D = -k\nabla\phi, \quad \text{in } \Omega_D, \tag{3}$$

$$\nabla\cdot\mathbf{u}_D = S, \quad \text{in } \Omega_D, \qquad (\mathbf{u}_D \text{ is given on } \partial\Omega_D) \tag{4}$$

where $\mathbf{u}_D = (u_D, v_D)$ is the Darcy velocity, k is the hydraulic conductivity coefficient, ϕ denotes the scaled pressure, and S is the external source/sink term.

To close the system (1)–(4), the governing equations must be coupled across the interface Γ by suitable conditions [22] in the following. Firstly, the mass conservation across Γ must be hold by

$$\mathbf{u}\cdot\mathbf{n} = \mathbf{u}_D\cdot\mathbf{n} \quad \text{on} \quad \Gamma. \tag{5}$$

The second interface condition is the balance of normal force across Γ as

$$2\nu\mathbf{n}\cdot\mathbf{D}\cdot\mathbf{n} = p - \phi \quad \text{on} \quad \Gamma, \tag{6}$$

where $\mathbf{D} = \frac{1}{2}\left(\nabla\mathbf{u} + \nabla^{\mathsf{T}}\mathbf{u}\right)$ is the deformation tensor. The pressure is allowed to be discontinuous across the interface. Lastly, since the fluid model is viscous, a condition on the tangential fluid velocity on Γ must be given. In general, the simplest assumption of no-slippage along the interface Γ is invalid due to the large deviation from experimental measurements [22]. Therefore the Beavers-Joseph-Saffman (BJS) interface condition [50, 51] is applied which states that the tangential component of the fluid velocity is proportional to the shear stress from the free fluid and the proportionality constant depends linearly on the square root of the permeability, i.e.,

$$\mathbf{u}\cdot\boldsymbol{\tau} = -\frac{2\sqrt{\tilde{k}}}{\alpha}\mathbf{n}\cdot\mathbf{D}\cdot\boldsymbol{\tau} \quad \text{on} \quad \Gamma, \tag{7}$$

where $\boldsymbol{\tau}$ is the unit tangent vector along the interface Γ, $\tilde{k} = \nu k$ and α are the positive constants. Here, the form $\sqrt{\tilde{k}}/\alpha$ has the physical meaning of friction coefficient.

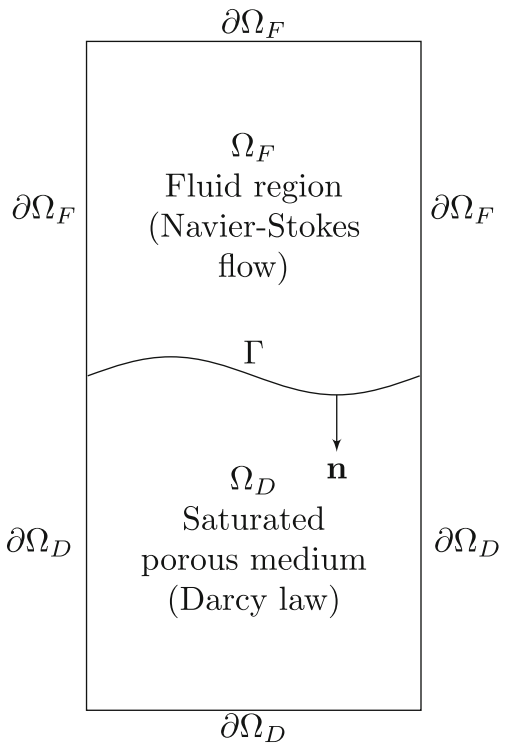

Fig. 1 Schematic representation of the coupled Navier-Stokes and Darcy system

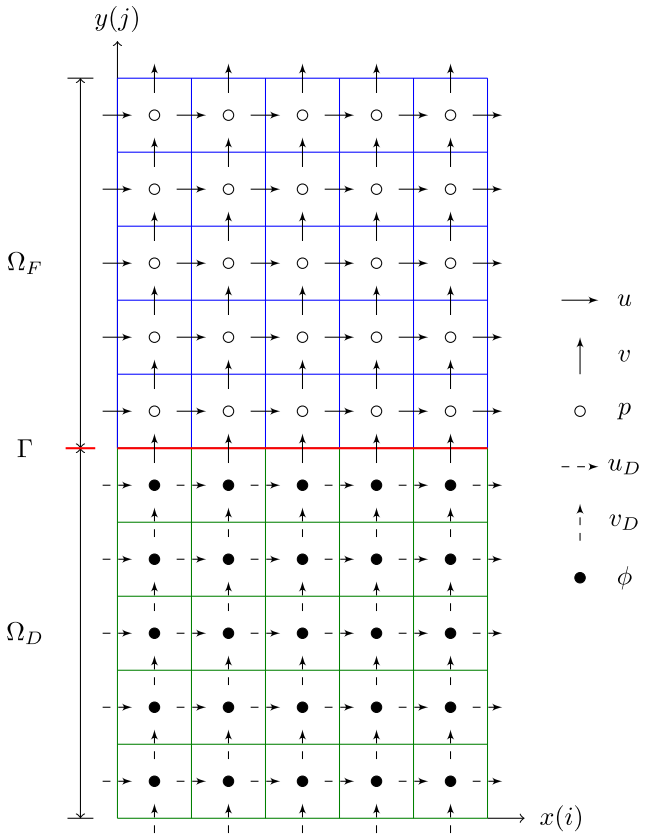

Fig. 2 Finite difference staggered grid

3 Finite difference discretization

To solve the coupled Navier-Stokes and Darcy flows with complex interface conditions, an underlying finite difference numerical scheme based on staggered grid is first described in this section. For the realistic applications with curved interface, the original curve can be approximated by a union of horizontal and vertical line segment interfaces. For simplicity, we assume Ω to be a rectangular domain $[0, L_x] \times [-L_y, L_y]$, where $\Omega_{\mathrm{F}} = [0, L_x] \times [0, L_y]$, and $\Omega_{\mathrm{D}} = [0, L_x] \times [-L_y, 0]$ in which L_x, L_y are positive constants. Therefore, the fluid-porous interface is a horizontal straight line at $y = 0$. Consequently, the interface outward normal vector is simply written as $\mathbf{n} = (0, -1)^{\mathsf{T}}$ and the interface conditions on Γ are simplified to

$$v = v_{\mathrm{D}} = v_{\Gamma} \tag{8}$$

$$2\nu \frac{\partial v_{\Gamma}}{\partial y} = p - \phi \tag{9}$$

$$u = \frac{\sqrt{\tilde{k}}}{\alpha} \left(\frac{\partial u}{\partial y} + \frac{\partial v_{\Gamma}}{\partial x} \right). \tag{10}$$

Similarly, in case of a vertical straight interface, the outward normal vector is $\mathbf{n} = (1, 0)^{\mathsf{T}}$, then the interface conditions on Γ are given by

$$u = u_{\mathrm{D}} = u_{\Gamma} \tag{11}$$

$$2\nu \frac{\partial u_{\Gamma}}{\partial x} = p - \phi \tag{12}$$

$$v = \frac{\sqrt{\tilde{k}}}{\alpha} \left(\frac{\partial v}{\partial x} + \frac{\partial u_{\Gamma}}{\partial y} \right). \tag{13}$$

For the clarity of presentation, the case with just a horizontal straight interface will be considered in the remainder of this section.

Let $x_i = (i - 1/2)\Delta x$, $y_j = (j - 1/2)\,\Delta y$ where the mesh sizes Δx and Δy are equal to L_x/M and L_y/N, respectively, with M and N as positive integers. The schematic representation of the finite difference discretization within the staggered grid framework is depicted in Fig. 2. As illustrated in Fig. 2, all the primitive variables are defined at different locations, with pressure p and scaled pressure ϕ defined at the cell centers, while the velocity components u, v, u_{D}, and v_{D} defined at the center of the cell faces. It should be noted that due to the staggered grid arrangement, the interface separating the fluid flow region and the porous medium is placed to be coinciding with the vertical velocity component $v_{\Gamma} = v = v_{\mathrm{D}}$. Therefore, to satisfy the interface conditions, an additional equation, i.e., Eq. 9, is required to solve for v_{Γ}.

Before discussing the spatial discretization for the governing equations and the interface conditions, an

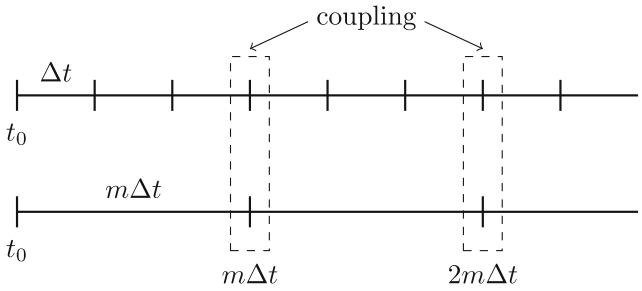

Fig. 3 Decoupled multi-step temporal integration scheme

extended projection method in light of the original projection method [48] is developed to calculate the primitive variables $\mathbf{u}$, p, $\mathbf{u}_\mathrm{D}$, ϕ at time level $n+1$ on the staggered grid. The projection method begins from a temporal discretization of the Navier-Stokes equations and Darcy law. Using the Euler implicit time stepping results in

$$\frac{\mathbf{u}^{n+1}-\mathbf{u}^n}{\Delta t}+\left(\mathbf{u}^n\cdot\nabla\right)\mathbf{u}^n-\nu\Delta\mathbf{u}^{n+1}+\nabla p^{n+1}=\mathbf{F}^{n+1}, \quad (14)$$

$$\nabla\cdot\mathbf{u}^{n+1}=0, \quad (15)$$

$$\mathbf{u}_\mathrm{D}^{n+1}=-k\nabla\phi^{n+1}, \quad (16)$$

$$\nabla\cdot\mathbf{u}_\mathrm{D}^{n+1}=S^{n+1}, \quad (17)$$

$$2\nu\frac{\partial v_\Gamma^{n+1}}{\partial y}|_\Gamma=\left(p^{n+1}-\phi^{n+1}\right)|_\Gamma. \quad (18)$$

The system of discretized equations is split into two sub-steps, i.e.,

$$\frac{\mathbf{u}^*-\mathbf{u}^n}{\Delta t}+\left(\mathbf{u}^n\cdot\nabla\right)\mathbf{u}^n-\nu\Delta\mathbf{u}^*=\mathbf{F}^{n+1}, \quad (19)$$

$$u^*=\frac{\sqrt{\tilde{k}}}{\alpha}\left(\frac{\partial u^*}{\partial y}+\frac{\partial v_\Gamma^n}{\partial x}\right)\quad\text{on}\quad\Gamma. \quad (20)$$

and

$$\begin{cases}\frac{\mathbf{u}^{n+1}-\mathbf{u}^*}{\Delta t}+\nabla p^{n+1}=0, & (21a)\\ \nabla\cdot\mathbf{u}^{n+1}=0, & (21b)\\ \mathbf{u}_\mathrm{D}^{n+1}=-k\nabla\phi^{n+1}, & (21c)\\ \nabla\cdot\mathbf{u}_\mathrm{D}^{n+1}=S^{n+1}, & (21d)\\ 2\nu\frac{\partial v_\Gamma^{n+1}}{\partial y}|_\Gamma=\left(p^{n+1}-\phi^{n+1}\right)|_\Gamma. & (21e)\end{cases}$$

By taking the divergence of Eq. 21a and 21c, and invoking Eq. 21b and 21d, system of Eq. 21 can be further reduced to

$$\begin{cases}\Delta p^{n+1}=\frac{1}{\Delta t}\nabla\cdot\mathbf{u}^*, & (22a)\\ -k\Delta\phi^{n+1}=S^{n+1}, & (22b)\\ 2\nu\frac{\partial v_\Gamma^{n+1}}{\partial y}|_\Gamma=\left(p^{n+1}-\phi^{n+1}\right)|_\Gamma. & (22c)\end{cases}$$

Equation 22a to 22c are to be solved by coupling each other with appropriate boundary conditions. Subsequently, $\mathbf{u}^{n+1}$ and $\mathbf{u}_\mathrm{D}^{n+1}$ are calculated through the following correction sub-step

$$\begin{cases}\mathbf{u}^{n+1}=\mathbf{u}^*-\Delta t\nabla p^{n+1}, & (23a)\\ \mathbf{u}_\mathrm{D}^{n+1}=-k\nabla\phi^{n+1}. & (23b)\end{cases}$$

The time-marching algorithm consists of three sub-steps for each time step: (i) the first sub-step accounts for viscous effects and computes the provisional velocity in the incompressible flow region. (ii) The second sub-step accounts for the incompressibility, and coupling of p, ϕ, v_Γ via interface conditions. (iii) Finally, the provisional velocity is corrected, and the velocity in the Darcy law region is updated. The present version of the projection method for Navier-Stokes equations shares the same spirit of SIMPLE algorithm [52, 53] but differs in some aspects where the latter algorithm is popularly used in some commercial CFD softwares. In the aforementioned sub-step (i), SIMPLE algorithm treats the nonlinear advection term semi-implicitly as $(\mathbf{u}^n\cdot\nabla)\mathbf{u}^*$ and an explicit term ∇p^n is added in the momentum equation. Thus, in step (2), the SIMPLE algorithm solves the incremental pressure Poisson equation rather than solving the pressure Poisson equation used in our present scheme. Since we have to solve the fluid pressure p and Darcy's scaled pressure ϕ together, SIMPLE algorithm for Navier-Stokes solver is not ultilized in the present study. For completeness of the numerical formulation, the spatial discretizations in both flow domains and their coupling at the interface are articulated in the remainder of this section.

Let $u_{i+1/2,j}$, $v_{i,j+1/2}$, and $p_{i,j}$ be denoted the discrete approximations of the flow velocity $u\left(x_{i+1/2},y_j\right)$,

Table 1 Grid refinement analysis of the fluid horizontal velocity u and Darcy horizontal velocity u_D at $T=1$

$M\times 2N$	$\|u_\mathrm{exact}-u\|_\infty$	Rate	$\|u_{\mathrm{D,exact}}-u_\mathrm{D}\|_\infty$	Rate
32×64	$8.484\times^{-03}$	–	$5.285\times^{-03}$	–
64×128	$4.963\times^{-03}$	0.77	$2.673\times^{-03}$	0.983
128×256	$2.694\times^{-03}$	0.88	$1.298\times^{-03}$	1.04
256×512	$1.398\times^{-03}$	0.95	$6.148\times^{-04}$	1.08

Time step is set as $\Delta t=h/2$ with $h=1/M$

Table 2 Grid refinement analysis of the fluid vertical velocity v and Darcy vertical velocity v_D at $T = 1$

$M \times 2N$	$\|v_{\text{exact}} - v\|_\infty$	Rate	$\|v_{D,\text{exact}} - v_D\|_\infty$	Rate
32×64	8.764×10^{-3}	–	7.457×10^{-3}	–
64×128	4.604×10^{-3}	0.93	4.200×10^{-3}	0.83
128×256	2.317×10^{-3}	0.99	2.221×10^{-3}	0.92
256×512	1.163×10^{-3}	0.99	1.134×10^{-3}	0.97

Time step is set as $\Delta t = h/2$ with $h = 1/M$

$v\left(x_i, y_{j+1/2}\right)$, and the pressure $p\left(x_i, y_i\right)$, respectively. In the similar context, let $(u_D)_{i+1/2,j}$, $(v_D)_{i,j+1/2}$, and $\phi_{i,j}$ denote the discrete approximations of the flow velocity $u_D\left(x_{i+1/2}, y_j\right)$, $v_D\left(x_i, y_{j+1/2}\right)$, and the scaled pressure $\phi\left(x_i, y_i\right)$, respectively. First, using the central differencing scheme, the momentum equation, i.e., Eq. 19, for provisional velocities u^* and v^* are discretized as

$$\begin{aligned}
&\frac{u^*_{i+1/2,j} - u^n_{i+1/2,j}}{\Delta t} + u^n_{i+1/2,j}\left(\frac{u^n_{i+3/2,j} - u^n_{i-1/2,j}}{2\Delta x}\right) \\
&\quad + v^n_{i+1/2,j}\left(\frac{u^n_{i+1/2,j+1} - u^n_{i+1/2,j-1}}{2\Delta y}\right) \\
&\quad - \nu\left[\frac{u^*_{i+3/2,j} - 2u^*_{i+1/2,j} + u^*_{i-1/2,j}}{(\Delta x)^2}\right. \\
&\quad \left. + \frac{u^*_{i+1/2,j+1} - 2u^*_{i+1/2,j} + u^*_{i+1/2,j-1}}{(\Delta y)^2}\right] \\
&\quad = f^{n+1}_{i+1/2,j}, \qquad (24)
\end{aligned}$$

for $(i, j) \in S_u$

$$= \left\{(i, j) \in \mathbb{Z}^2 | 1 \le i \le M-1, 1 \le j \le N\right\},$$

and

$$\begin{aligned}
&\frac{v^*_{i,j+1/2} - v^n_{i,j+1/2}}{\Delta t} + v^n_{i,j+1/2}\left(\frac{v^n_{i,j+3/2} - v^n_{i,j-1/2}}{2\Delta y}\right) \\
&\quad + u^n_{i,j+1/2}\left(\frac{v^n_{i+1,j+1/2} - v^n_{i-1,j+1/2}}{2\Delta x}\right) \\
&\quad - \nu\left[\frac{v^*_{i+1,j+1/2} - 2v^*_{i,j+1/2} + v^*_{i-1,j+1/2}}{(\Delta x)^2}\right. \\
&\quad \left. + \frac{v^*_{i,j+3/2} - 2v^*_{i,j+1/2} + v^*_{i,j-1/2}}{(\Delta y)^2}\right] \\
&\quad = g^{n+1}_{i,j+1/2}, \qquad (25)
\end{aligned}$$

for $(i, j) \in S_v$

$$= \left\{(i, j) \in \mathbb{Z}^2 | 1 \le i \le M, 1 \le j \le N-1\right\},$$

respectively. The non-linear advection terms are discretized explicitly while the diffusion terms are treated implicitly to assist stability. In this configuration, the coupling interface is located along $j = 1/2$ and is coincided with the vertical velocity component $(v_\Gamma)_{i,1/2}$. Therefore, additional treatments are required to impose on Eqs. 24 and 25 in order to include the coupling interface conditions.

Considering Eq. 24, the u^* component at $j = 1$ adjacent to the interface is given by

$$\begin{aligned}
&\frac{u^*_{i+1/2,1} - u^n_{i+1/2,1}}{\Delta t} + u^n_{i+1/2,1}\left(\frac{u^n_{i+3/2,1} - u^n_{i-1/2,1}}{2\Delta x}\right) \\
&\quad + v^n_{i+1/2,1}\left(\frac{u^n_{i+1/2,2} - u^n_{i+1/2,0}}{2\Delta y}\right) \\
&\quad - \nu\left[\frac{u^*_{i+3/2,1} - 2u^*_{i+1/2,1} + u^*_{i-1/2,1}}{(\Delta x)^2}\right. \\
&\quad \left. + \frac{u^*_{i+1/2,2} - 2u^*_{i+1/2,1} + u^*_{i+1/2,0}}{(\Delta y)^2}\right] \\
&\quad = f^{n+1}_{i+1/2,1}, \\
&i = 1, \cdots, M-1, \qquad (26)
\end{aligned}$$

where the ghost nodes $u^*_{i+1/2,0}$ and $u^n_{i+1/2,0}$ are required to be evaluated. The Beavers-Joseph-Saffman condition (10) is approximated and discretized at $j = 1/2$ as

$$\begin{aligned}
\frac{u^*_{i+1/2,1} + u^*_{i+1/2,0}}{2} &= \frac{\sqrt{\tilde{k}}}{\alpha}\left(\frac{u^*_{i+1/2,1} - u^*_{i+1/2,0}}{\Delta y}\right) \\
&\quad + \frac{\sqrt{\tilde{k}}}{\alpha}\left(\frac{(v_\Gamma)^n_{i+1,1/2} - (v_\Gamma)^n_{i,1/2}}{\Delta x}\right). \qquad (27)
\end{aligned}$$

Table 3 Grid refinement analysis of the fluid vertical velocity at the interface v_Γ at $T = 1$

$M \times 2N$	$\|v_{\Gamma,\text{exact}} - v_\Gamma\|_\infty$	Rate
32×64	9.372×10^{-03}	–
64×128	$4.830 \times 10^{-03-03}$	0.96
128×256	$2.402 \times 10^{-03-03}$	1.01
256×512	$1.189 \times 10^{-03-03}$	1.02

Time step is set as $\Delta t = h/2$ with $h = 1/M$

Table 4 Grid refinement analysis of the pressure p and scaled pressure ϕ at $T = 1$

$M \times 2N$	$\|p_{\text{exact}} - p\|_\infty$	Rate	$\|\phi_{\text{exact}} - \phi\|_\infty$	Rate
32×64	3.149×10^{-1}	-	1.590×10^{-3}	-
64×128	2.228×10^{-1}	0.50	7.901×10^{-4}	1.01
128×256	1.562×10^{-1}	0.51	3.778×10^{-4}	1.06
256×512	1.093×10^{-1}	0.52	1.779×10^{-4}	1.09
$M \times 2N$	$\|p_{\text{exact}} - p\|_2$	Rate	$\|\phi_{\text{exact}} - \phi\|_2$	Rate
32×64	9.434×10^{-2}	–	3.746×10^{-4}	–
64×128	5.322×10^{-2}	0.83	1.641×10^{-4}	1.19
128×256	2.935×10^{-2}	0.86	7.165×10^{-5}	1.20
256×512	$1.601 - \times 10^{-2}$	0.87	3.150×10^{-5}	1.19

Time step is set as $\Delta t = h/2$ with $h = 1/M$

This yields the ghost node $u^*_{i+1/2,0}$

$$u^*_{i+1/2,0} = \left(\frac{2\sqrt{\tilde{k}}/\alpha\Delta y - 1}{2\sqrt{k}/\alpha\Delta y + 1}\right) u^*_{i+1/2,1} + \frac{2\sqrt{\tilde{k}}/\alpha\Delta x}{2\sqrt{\tilde{k}}/\alpha\Delta y + 1}\left((v_\Gamma)^n_{i+1,1/2} - (v_\Gamma)^n_{i,1/2}\right). \tag{28}$$

Similarly, the ghost node $u^n_{i+1/2,0}$ can be approximated in the identical manner.

Now, considering Eq. 25 on the other hand, the v^* component at $j = 3/2$ adjacent to the interface is given by

$$\begin{aligned}\frac{v^*_{i,3/2} - v^n_{i,3/2}}{\Delta t} &+ u^n_{i,3/2}\left(\frac{v^n_{i+1,3/2} - v^n_{i-1,3/2}}{2\Delta x}\right) \\ &+ v^n_{i,3/2}\left(\frac{v^n_{i,5/2} - (v_\Gamma)^n_{i,1/2}}{2\Delta y}\right) \\ &- \nu\left[\frac{v^*_{i+1,3/2} - 2v^*_{i,3/2} + v^*_{i-1,3/2}}{(\Delta x)^2}\right. \\ &\left. + \frac{v^*_{i,5/2} - 2v^*_{i,3/2} + (v_\Gamma)^*_{i,1/2}}{(\Delta y)^2}\right] = g^{n+1}_{i,3/2}, \\ & i = 1, \cdots, M. \end{aligned} \tag{29}$$

The $(v_\Gamma)^n_{i,1/2}$ prevailing at previous time step n is employed for the explicit discretization of advection term. However, the $(v_\Gamma)^*_{i,1/2}$ term in the implicit diffusion term can be obtained from Eq. 9 and approximated by first-order one-sided difference as

$$2\nu\left(\frac{v^*_{i,3/2} - (v_\Gamma)^*_{i,1/2}}{\Delta y}\right) = p^n_{i,1} - \phi^n_{i,0}, \ \ i = 1, \cdots, M. \tag{30}$$

Next, for the coupled system of Eq. 22, the spatial discretization yields

$$\begin{aligned}\frac{p^{n+1}_{i+1,j} - 2p^{n+1}_{i,j} + p^{n+1}_{i-1,j}}{(\Delta x)^2} &+ \frac{p^{n+1}_{i,j+1} - 2p^{n+1}_{i,j} + p^{n+1}_{i,j-1}}{(\Delta y)^2} \\ &= \frac{1}{\Delta t}\left[\frac{u^*_{i+1/2,j} - u^*_{i-1/2,j}}{\Delta x}\right. \\ &\left. + \frac{v^*_{i,j+1/2} - v^*_{i,j-1/2}}{\Delta y}\right], \end{aligned} \tag{31}$$

for $(i, j) \in S$

$$= \left\{(i, j) \in \mathbb{Z}^2 | 1 \le i \le M, 1 \le j \le N\right\},$$

$$\frac{\frac{\phi^{n+1}_{i+1,j} - 2\phi^{n+1}_{i,j} + \phi^{n+1}_{i-1,j}}{(\Delta x)^2}}{+\frac{\phi^{n+1}_{i,j+1} - 2\phi^{n+1}_{i,j} + \phi^{n+1}_{i,j-1}}{(\Delta y)^2}} = -\frac{S^{n+1}_{i,j}}{k}, \tag{32}$$

for $(i, j) \in D$

$$= \left\{(i, j) \in \mathbb{Z}^2 | 1 \le i \le M, -N + 1 \le j \le 0\right\},$$

Table 5 Grid refinement analysis of the scaled pressure gradient ϕ_x and ϕ_y at $T = 1$

$M \times 2N$	$\|\phi_{x,\text{exact}} - \phi_x\|_2$	Rate	$\|\phi_{y,\text{exact}} - \phi_y\|_2$	Rate
32×64	1.253×10^{-3}	–	1.154×10^{-3}	–
64×128	5.748×10^{-4}	1.12	5.466×10^{-4}	1.08
128×256	2.618×10^{-4}	1.13	2.535×10^{-4}	1.11
256×512	1.200×10^{-4}	1.13	1.174×10^{-4}	1.11

Time step is set as $\Delta t = h/2$ with $h = 1/M$

Table 6 Grid refinement analysis of the fluid horizontal velocity u and Darcy horizontal velocity u_D at $T = 1$

$M \times 2N$	$\|u_{\text{exact}} - u\|_\infty$	Rate	$\|u_{\text{D,exact}} - u_D\|_\infty$	Rate
32×64	4.145×10^{-4}	–	1.584×10^{-4}	–
64×128	1.080×10^{-4}	1.94	$3.446 \times 10{-5}$	2.20
128×256	2.754×10^{-5}	1.97	$7.911 \times 10{-6}$	2.12
256×512	6.951×10^{-6}	1.99	$2.133 \times 10{-6}$	1.89

Time step is set as $\Delta t = h^2/2$ with $h = 1/M$

$$2\nu\left(\frac{v^{n+1}_{i,3/2}-(v_\Gamma)^{n+1}_{i,1/2}}{\Delta y}\right)=p^{n+1}_{i,1}-\phi^{n+1}_{i,0},\quad i=1,\cdots,M. \tag{33}$$

Note that at the current stage, $v^{n+1}_{i,3/2}$ is unknown. In this case, the correction sub-step Eq. 23 must be invoked, i.e.,

$$v^{n+1}_{i,3/2} = v^{*}_{i,3/2} - \Delta t\left(\frac{p^{n+1}_{i,2}-p^{n+1}_{i,1}}{\Delta y}\right),\quad i=1,\cdots,M. \tag{34}$$

Hence, Eq. 33 is written as

$$\begin{aligned}2\nu\frac{v^{*}_{i,3/2}-(v_\Gamma)^{n+1}_{i,1/2}}{\Delta y} &= p^{n+1}_{i,1}-\phi^{n+1}_{i,0}\\ &\quad+\frac{2\nu\Delta t}{(\Delta y)^2}\left(p^{n+1}_{i,2}-p^{n+1}_{i,1}\right),\\ i &= 1,\cdots,M.\end{aligned} \tag{35}$$

To impose the coupling interface conditions and boundary conditions, additional treatments are required for Eqs. 31 and 32. Note that along the interface $j = 1/2$ in i direction, where all the variables of p^{n+1} are located at the cell center along $j = 1$, Eq. 31 is coupled with $(v_\Gamma)^{n+1}_{i,1/2}$ as

$$\begin{aligned}\frac{p^{n+1}_{i+1,1}-2p^{n+1}_{i,1}+p^{n+1}_{i-1,1}}{(\Delta x)^2}+\frac{p^{n+1}_{i,2}-2p^{n+1}_{i,1}+p^{n+1}_{i,0}}{(\Delta y)^2}&\\ =\frac{1}{\Delta t}\left[\frac{u^{*}_{i+1/2,1}-u^{*}_{i-1/2,1}}{\Delta x}\right.&\\ \left.+\frac{v^{*}_{i,3/2}-(v_\Gamma)^{n+1}_{i,1/2}}{\Delta y}\right].&\end{aligned} \tag{36}$$

Here, the ghost value $p^{n+1}_{i,0}$ can be obtained easily by approximating zero Neumann boundary condition on the interface Γ. On the other hand, ϕ^{n+1} located at the cell center along $j = 0$ adjacent to the interface is given by

$$\frac{\phi^{n+1}_{i+1,0}-2\phi^{n+1}_{i,0}+\phi^{n+1}_{i-1,0}}{(\Delta x)^2}+\frac{\phi^{n+1}_{i,1}-2\phi^{n+1}_{i,0}+\phi^{n+1}_{i,-1}}{(\Delta y)^2}=-\frac{S^{n+1}_{i,0}}{k}, \tag{37}$$

where the ghost value $\phi^{n+1}_{i,1}$ is evaluated by direct substitution of the gradient at the interface Γ as

$$\frac{\phi^{n+1}_{i,1}-\phi^{n+1}_{i,0}}{\Delta y}=-\frac{1}{k}(v_\Gamma)^{n+1}_{i,1/2}, \tag{38}$$

which is also coupled with $(v_\Gamma)^{n+1}_{i,1/2}$.

Finally, in the correction sub-step, u^{n+1} and v^{n+1} in incompressible fluid region are computed as

$$u^{n+1}_{i+1/2,j} = u^{*}_{i+1/2,j} - \Delta t\left(\frac{p^{n+1}_{i+1,j}-p^{n+1}_{i,j}}{\Delta x}\right), \tag{39}$$

for $(i, j) \in S_u$,

$$v^{n+1}_{i,j+1/2} = v^{*}_{i,j+1/2} - \Delta t\left(\frac{p^{n+1}_{i,j+1}-p^{n+1}_{i,j}}{\Delta y}\right), \tag{40}$$

for $(i, j) \in S_v$. The correction sub-step ensures that u^{n+1} and v^{n+1} in the incompressible fluid flow region satisfy the divergence-free kinematic constraint. Concurrently, u^{n+1}_D and v^{n+1}_D in the porous medium region are also updated, i.e.

$$(u_D)^{n+1}_{i+1/2,j} = -k\left(\frac{\phi^{n+1}_{i+1,j}-\phi^{n+1}_{i,j}}{\Delta x}\right), \tag{41}$$

Table 7 Grid refinement analysis of the fluid vertical velocity v and Darcy vertical velocity v_D at $T = 1$

$M \times 2N$	$\|v_{\text{exact}} - v\|_\infty$	Rate	$\|v_{\text{D,exact}} - v_D\|_\infty$	Rate
32×64	3.287×10^{-4}	–	2.571×10^{-4}	–
64×128	8.396×10^{-5}	1.97	6.966×10^{-5}	1.88
128×256	2.114×10^{-5}	1.99	1.788×10^{-5}	1.96
256×512	5.275×10^{-6}	2.00	4.398×10^{-6}	2.02

Time step is set as $\Delta t = h^2/2$ with $h = 1/M$

Table 8 Grid refinement analysis of the fluid vertical velocity at the interface v_Γ at $T = 1$

$M \times 2N$	$\|v_{\Gamma,\text{exact}} - v_\Gamma\|_\infty$	Rate
32×64	3.699×10^{-4}	–
64×128	9.458×10^{-5}	1.97
128×256	2.378×10^{-5}	1.99
256×512	5.900×10^{-6}	2.01

Time step is set as $\Delta t = h^2/2$ with $h = 1/M$

for $(i, j) \in D_u$

$$= \left\{(i, j) \in \mathbb{Z}^2 | 1 \le i \le M - 1, -N + 1 \le j \le 0\right\},$$

$$(v_D)^{n+1}_{i,j+1/2} = -k\left(\frac{\phi^{n+1}_{i,j+1} - \phi^{n+1}_{i,j}}{\Delta y}\right), \tag{42}$$

for $(i, j) \in D_v$

$$= \left\{(i, j) \in \mathbb{Z}^2 | 1 \le i \le M, -N + 2 \le j \le 0\right\}.$$

The aforementioned discretization framework still holds in case of straight vertical interface $\mathbf{n} = (1, 0)^\mathsf{T}$ by switching the "role" between the horizontal u and vertical v velocity components adjacent to the interface. The vertical interface separating the fluid flow region and the porous medium is placed to be coinciding with the horizontal velocity component $u_\Gamma = u = u_\text{D}$. Therefore, Eq. 12 is required to solve for u_Γ. The discretization for u_Γ follows exactly Eq. 33. The Beavers-Joseph-Saffman condition (13) is discretized on Γ and imposed as an implicit boundary condition for v^* equations similar to Eq. 26.

In the majority of real-world situations, the fluid velocity magnitude in the incompressible fluid region is marginally higher than the fluid velocity magnitude in the porous medium. Since the coupled system evolves on different time scales, the multi-step temporal integration scheme [33] can be adopted. By introducing two temporal grids, the coupled system of Eqs. 31 and 33 is decoupled from Eq. 32, i.e.,

$$2\nu\frac{v^*_{i,3/2} - (v_\Gamma)^{n+1}_{i,1/2}}{\Delta y} = p^{n+1}_{i,1} - \phi^m_{i,0} + \frac{2\nu\Delta t}{(\Delta y)^2}\left(p^{n+1}_{i,2} - p^{n+1}_{i,1}\right), \tag{43}$$

where the time level n represents the fine time step and time level m represents the coarse time step. In this case, the incompressible fluid flow solutions are computed with a fine time step Δt and the porous medium solutions are computed with a coarse time step $m\Delta t$ where $m \ge 1$ is the ratio between the coarse and fine time steps. Figure 3 shows the two temporal grids schematically. The coupled system of Eqs. 31 to 33 is only solved once at every coarse time level $m\Delta t$. Note that the ratio m is a problem-dependent parameter which depends on the local characteristic of the flows. It is possible that the ratio m can be set dynamically and adaptively throughout the simulation.

4 Numerical results

4.1 Accuracy check of the present method

To validate and to check the numerical convergence of the present numerical method, a grid refinement analysis is conducted by constructing an analytic solution. Consider the Navier-Stokes flow in $0 \le x \le 1, 1 \le y \le 2$ and the Darcy flow in $0 \le x \le 1, 0 \le y \le 1$, the exact solution is given by

$$u = e^{-t}\left[(y-1)^2 + x(y-1) + 3x - 1\right], \tag{44}$$

$$v = e^{-t}\left[x(x-1) - 0.5(y-1)^2 - 3y + 1\right], \tag{45}$$

$$p = e^{-t}\left(2x + y - 1\right), \tag{46}$$

$$u_D = e^{-t}\left[(x-1)(y-1) + x(y-1) - 2\right], \tag{47}$$

Table 9 Grid refinement analysis of the pressure p and scaled pressure ϕ at $T = 1$

$M \times 2N$	$\|p_\text{exact} - p\|_\infty$	Rate	$\|\phi_\text{exact} - \phi\|_\infty$	Rate
32×64	7.446×10^{-2}	–	5.155×10^{-5}	–
64×128	3.693×10^{-2}	1.01	1.217×10^{-5}	2.08
128×256	1.835×10^{-2}	1.01	2.832×10^{-6}	2.11
256×512	9.144×10^{-3}	1.01	7.792×10^{-7}	1.86
$M \times 2N$	$\|p_\text{exact} - p\|_2$	Rate	$\|\phi_\text{exact} - \phi\|_2$	Rate
32×64	3.229×10^{-2}	–	2.028×10^{-5}	–
64×128	1.553×10^{-2}	1.06	4.892×10^{-6}	2.05
128×256	7.613×10^{-3}	1.03	1.187×10^{-6}	2.04
256×512	3.768×10^{-3}	1.01	2.914×10^{-7}	2.03

Time step is set as $\Delta t = h^2/2$ with $h = 1/M$

Table 10 Grid refinement analysis of the scaled pressure gradient ϕ_x and ϕ_y at $T = 1$

$M \times 2N$	$\|\phi_{x,\text{exact}} - \phi_x\|_2$	Rate	$\|\phi_{y,\text{exact}} - \phi_y\|_2$	Rate
32×64	3.321×10^{-5}	–	3.025×10^{-5}	–
64×128	6.781×10^{-6}	2.29	6.426×10^{-6}	2.24
128×256	1.212×10^{-6}	2.48	1.168×10^{-6}	2.46
256×512	2.746×10^{-7}	2.14	2.672×10^{-7}	2.13

Time step is set as $\Delta t = h^2/2$ with $h = 1/M$

$$v_D = e^{-t}\left[x(x-1) - (y-1)^2 - 2\right], \tag{48}$$

$$\phi = e^{-t}\left[x(1-x)(y-1) + \frac{(y-1)^3}{3} + 2x + 2y + 4\right], \tag{49}$$

with parameters $\nu = 1$, $k = 1$, and $\alpha = 1$. In addition, the exact solution also satisfies the interface conditions Eqs.8 to 10. It should be noted that along the interface $y = 1$, the aforementioned solution has discontinuous pressure and non-zero velocity. The convergence tests are carried out for all the primary variables using four levels of grid-resolution starting from $M \times 2N = 32 \times 64$ with uniform mesh size $\Delta x = \Delta y = h$, time step $\Delta t = h/2$ and $\Delta t = h^2/2$. The computations are performed with time-marching up to time $T = 1.0$. For the case with $\Delta t = h/2$, the errors and convergent rates in L_∞-norm for u and u_D, v and v_D, v_Γ, p and ϕ are summarized in Tables 1, 2, 3, and 4, respectively. In addition, the errors and convergent rates in L_2-norm for p, ϕ, ϕ_x, and ϕ_y are summarized in Tables 4 and 5.

In a same manner, the corresponding errors and convergent rates in L_∞-norm for the case with $\Delta t = h^2/2$ are summarized in Tables 6, 7, 8, and 9. In addition, the corresponding errors and convergent rates in L_2-norm are summarized in Tables 9 and 10. For the case Δt proportional to h, the fluid velocity u and v, Darcy velocities u_D and v_D, vertical velocity at the interface v_Γ, and scaled pressure ϕ are first-order accurate in L_∞-norm, whereas the pressure p is only half-order accurate in L_∞-norm. Pressure p, scaled pressure ϕ, and its gradients ϕ_x, ϕ_y are first-order accurate in L_2-norm. This first-order accuracy for the velocity is due to the choice of first-order temporal discretization of the projection method. However, for the case of Δt proportional to h^2, the fluid velocities u and v, Darcy velocities u_D and v_D, vertical velocity at the interface v_Γ, as well as scaled pressure ϕ are second-order accurate in L_∞-norm, whereas the pressure p is first-order accurate in L_∞-norm and L_2-norm. Scaled pressure ϕ and its gradients ϕ_x, ϕ_y are second-order accurate in L_2-norm.

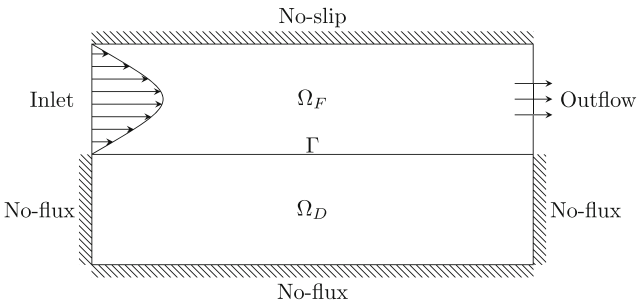

Fig. 4 Initial and boundary conditions which represent the percolation of waters of hydrological basins through rocks and sand

4.2 Percolation of fluid through porous medium

A physical example is used to demonstrate the capability of the developed numerical algorithm. Consider the domains $\Omega_\text{F} = [0, 8] \times [1, 2]$ and $\Omega_\text{D} = [0, 8] \times [0, 1]$, the initial and boundary conditions are depicted in Fig. 4. This canonical case may represent the percolation of fluid through porous medium [33]. The inlet boundary condition at the left boundary of the incompressible fluid flow region $\partial\Omega_\text{F} = \{0\} \times [1, 2]$ is given by

$$u = U\left(1 - 4\,(y - 1.5)^2\right), \quad v = 0 \tag{50}$$

where $U = 10$ in this case. The outflow condition is prescribed at the right boundary and no-slip boundary is prescribed at the top boundary of the incompressible fluid flow region $\partial\Omega_\text{F} = \{8\} \times [1, 2]$. For the remaining boundaries of the porous medium domain, the no-flux boundary condition $\nabla\phi \cdot \mathbf{n} = 0$ is imposed. The initial velocities in Ω_F and Ω_D are zero. The computation is performed with time-marching, starting from the initial condition to the steady-state using mesh size of $\Delta x = \Delta y = h = 1/60$ and time step of $\Delta t = h^2/2$. The steady-state solution is justified by assessing the convergence of the primitive variables.

Figure 5 depicts the comparison of the flow field using different hydraulic conductivity coefficients $k = 1.0$ (Fig. 5a) and $k = 0.01$ (Fig. 5b). In both cases, the fluid from the incompressible flow region Ω_F flows into the porous medium region Ω_D until the mass flux across the interface Γ has reached the steady-state. Subsequently, the

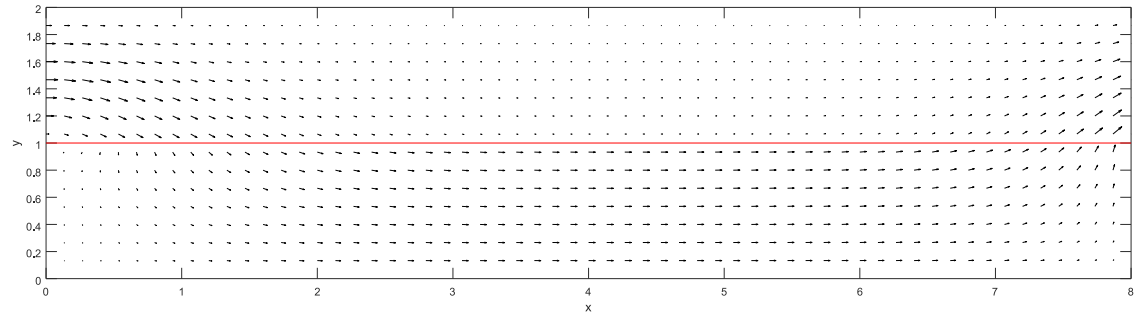

(a) $k = 1.0$

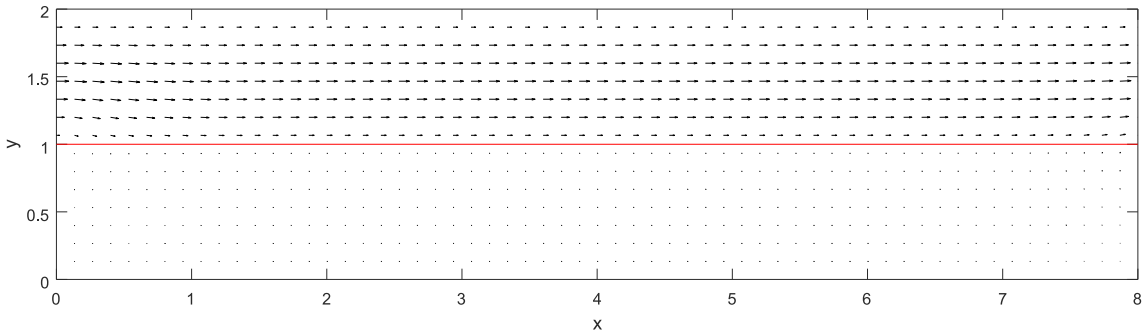

(b) $k = 0.01$

Fig. 5 Comparison of velocity vectors with relative magnitude between the case **a** $k = 1.0$ and the case **b** $k = 0.01$

boundary layer along the top boundary due to the no-slip condition, and along the interface Γ in the incompressible flow region Ω_F due to the BJS interface condition, continue to develop toward steady-state. The primary discrepancy between the two cases is the magnitude of the mass flux across the interface Γ. Figure 6 illustrates the comparison of normalized velocity v_Γ/U profiles along the interface Γ using different k values starting from $k = 0.0001$ to $k = 1.0$. Due to the conservation of mass, the sum of the mass flow across the interface Γ must be zero. Table 11 justifies that the projection method enforces the discrete divergence-free conditions, and the mass balance error $\| \int_\Gamma v_\Gamma \mathrm{d}h \|$ across the interface Γ is up to the machine accuracy. Since k is proportional to permeability, the magnitude of normalized velocity flows from the incompressible fluid region into the porous medium region increases as the value of k increases. To illustrate this, Fig. 7 depicts the mass flux across the interface Γ normalized by the inlet mass flux. It is noted that the normalized mass flux increases significantly with permeability proportional to k.

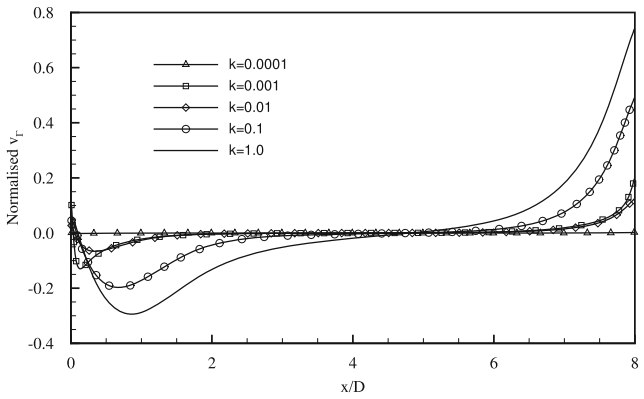

Fig. 6 Normalized velocity v_Γ/U profiles along the interface Γ using different k values starting from $k = 0.0001$ to $k = 1.0$

The accuracy of the multi-step temporal scheme is evaluated herein using the preceding case study with identical boundary conditions and initial conditions. Table 12 summarizes the comparison of normalized mass flux across the interface using the coarse to fine time step ratio $m = 1, 2, 3, 5$ with $k = 1.0, 0.001, 0.0001$. The predicted normalized mass fluxes for $m = 2, 3, 5$ are consistent with the fully coupled case $m = 1$. By decoupling the system of Eqs. 31 to 33 and only solve once at every coarse time level $m\Delta t$, the computational cost can be reduced without degrading the accuracy.

Table 11 Mass balance error $\| \int_\Gamma v_\Gamma \mathrm{d}h \|$ across the interface Γ

k	Mass balance error on Γ
$k = 1.0$	8.750×10^{-13}
$k = 0.1$	1.145×10^{-13}
$k = 0.01$	4.297×10^{-14}
$k = 0.001$	6.886×10^{-15}
$k = 0.0001$	8.058×10^{-16}

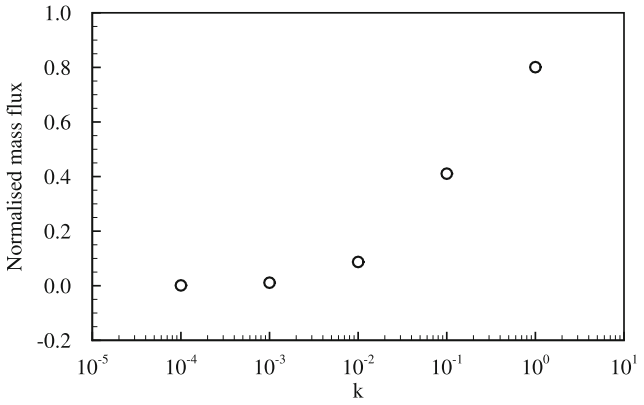

Fig. 7 Normalized mass flux across the interface Γ

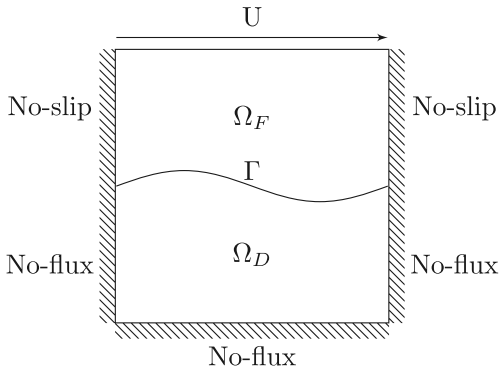

Fig. 8 Initial and boundary conditions which represent the groundwater system

4.3 Coupled surface and subsurface flows

An example of coupled surface and subsurface flows (e.g., groundwater system) is exercised to demonstrate the numerical simulation with an arbitrary interface. As depicted in Fig. 8, a domain $\Omega = [0, 1] \times [0, 1]$ with a reference length $L = 1.0$ is separated by an interface Γ, where the top half Ω_F denotes a lake or aquarium (surface flow) and the bottom half Ω_D denotes an aquifer with $k = 1.0$ (subsurface flow).

The domain is partitioned into these two regions by conforming the staggered grid approximately to the prescribed interface $\Gamma(x) = 0.5 + 0.2 \sin(1.5\pi x)$ (refer to Fig. 9) with horizontal and vertical line segments. Subsequently, the proposed numerical formulation can be applied directly with minor modifications while retaining its simplicity. Now, the u and v equations at each cell adjacent to the interface are imposed with interface conditions depending on the local orientation of the interface i.e. horizontal $\mathbf{n} = (0, -1)^T$ or vertical $\mathbf{n} = (1, 0)^T$. In particular, the normal velocity components at the interface are computed using the same formulation, i.e., Eq. 6. On the other hand, the tangential velocity components at the interface are considered implicitly as the ghost nodes for the Navier-Stokes equation, i.e., Eq. 7. The discretizations exactly follow Eqs. 33 and 28 respectively.

The flow is driven by applying a drag force ($Re_U = 100$) along top boundary $\partial\Omega_F = [0, 1] \times \{1\}$. No-slip boundary condition is imposed on the remaining boundaries $\partial\Omega_F$ and no-flux boundary condition is imposed on $\partial\Omega_D$. The velocities of Ω_F and Ω_D are initially zero. The computation is performed with time-marching, starting from the initial

Table 12 Comparison of normalized mass flux across the interface using the coarse to fine time-step ratio $m = 1, 2, 3, 5$ with $k = 1.0, 0.001, 0.0001$

Ratio	$k = 0.0001$	$k = 0.001$	$k = 1.0$
$m = 1$	1.183×10^{-4}	1.114×10^{-2}	8.21×10^{-1}
$m = 2$	1.183×10^{-4}	1.114×10^{-2}	8.21×10^{-1}
$m = 3$	1.038×10^{-4}	1.114×10^{-2}	8.21×10^{-1}
$m = 5$	1.979×10^{-4}	1.535×10^{-2}	8.21×10^{-1}

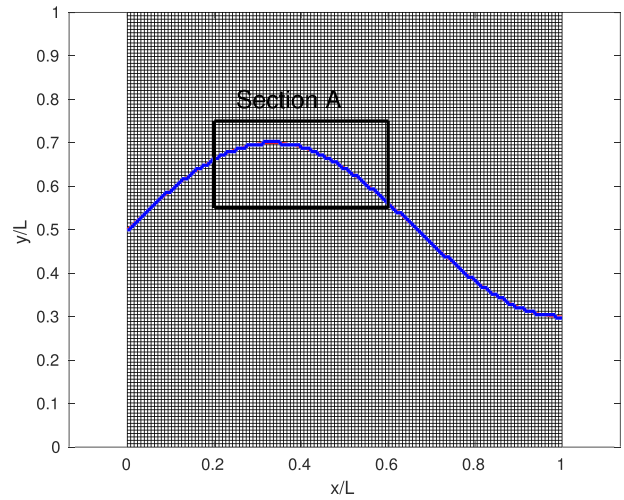

(a) Partitioned domain

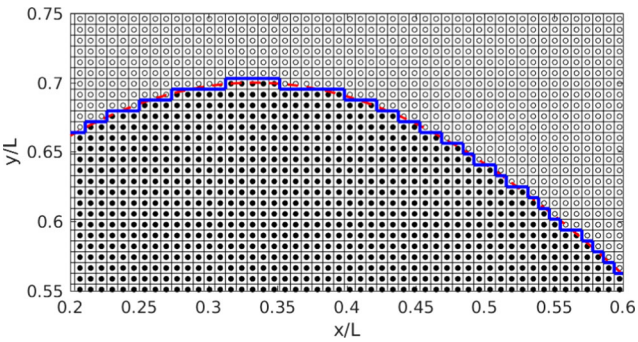

(b) Section A

Fig. 9 **a** Partitioned domain. **b** Section A view A (white circle indicates cell center for incompressible flows region and black circle indicates cell center for Darcy flows region). The domain is separated by conforming the staggered grid to the prescribed interface (indicated by a dashed line)

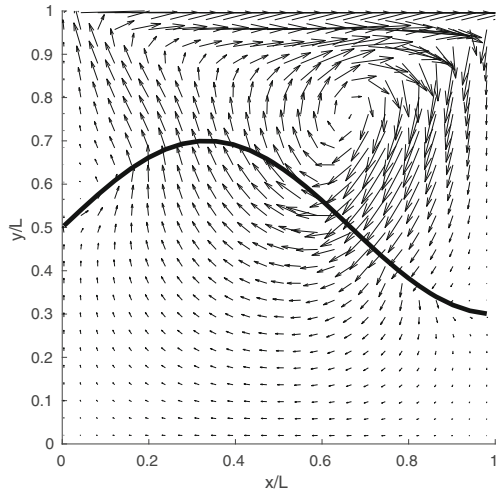

Fig. 10 Velocity vector plot of a shear-driven recirculation flow. The domain is separated by a interface, where the top half surface flow and the bottom half denotes subsurface flow with $k = 1.0$

condition to the steady-state using a mesh size of $\Delta x = \Delta y = h = 1/128$ and a time-step of $\Delta t = (h/2)^2$. A complex recirculation flow is formed within the domain, and the steady-state solution is determined by monitoring the convergence of the primitive variables.

A recirculation flow can be observed in Fig. 10. A shear-driven primary vortex is formed nearby the geometric center of the domain. Furthermore, two secondary vortices can be identified nearby the left and right boundaries adjacent to the interface. The secondary vortices are attributed to the primary recirculation flow, the discontinuous tangential velocity (BJS condition) across the interface, and the no-slip boundary condition. While the normal velocity is continuous and the mass flux is conserved, the surface fluid flows into the aquifer through the interface and decelerates due to the permeability. Subsequently, the fluid percolates and recirculates back toward the surface through the interface.

5 Conclusion

The fluid transport phenomena across the interface between an incompressible fluid region and a porous medium have received increasing attention both from the mathematical and the numerical points of view. While the numerical schemes of each sub-problem are well-known and well-developed, the development of a high-fidelity numerical algorithm for the coupled problem is challenging. In the present study, the Navier-Stokes equations and the Darcy law, with complex interface conditions, are used to describe the coupled incompressible flow and porous medium system. A finite difference projection method is developed within a staggered grid framework to solve the coupled system in a segregated manner using primitive variables. Numerical simulations are carried out for the model problem with a designed analytical solution and an application to demonstrate the order of convergence and its capability. The grid refinement analysis shows that, for the case Δt proportional h^2, all primitive variables are second-order accurate in L_∞-norm, except pressure which is first-order accurate in L_∞-norm and L_2-norm. Scaled pressure ϕ and its gradients ϕ_x, ϕ_y are second-order accurate in L_2-norm. While for the case Δt proportional h, only pressure is half-order accurate in L_∞-norm, whereas all other primitive variables are first-order accurate. Pressure p, scaled pressure ϕ, and its gradients ϕ_x, ϕ_y are first-order accurate in L_2-norm. The proposed method provides a fundamental and flexible way in solving coupled Navier-Stokes and Darcy flow problems and it is readily extendible to multi-physics fluid flows for a wide range of applications including physiology, urban climate, and various engineering analysis.

Funding information The work of M. C. Lai was supported in part by the Ministry of Science and Technology of Taiwan under research grant MOST-104-2115-M-009-014-MY3. M. C. Shiue was supported in part by the grant MOST-106-2115-M-009-011-MY2. K.C. Ong was supported in part by the National Center for Theoretical Sciences and National Chiao Tung University during his visit.

References

1. Arbogast, T., Brunson, D.S.: A computational method for approximating a Darcy-Stokes system governing a vuggy porous medium. Comput. Geosci. **11**, 207–218 (2007)
2. Urquiza, J., N'Dri, D., Garon, A., Delfour, M.: Coupling Stokes and Darcy equations. Appl. Numer. Math. **58**, 525–538 (2008)
3. Karper, T., Mardal, K.-A., Winther, R.: Unified finite element discretizations of coupled Darcy Stokes flow. Numerical Methods for Partial Differential Equations **25**, 311–326 (2009)
4. Cao, Y., Gunzburger, M., Hu, X., Hua, F., Wang, X., Zhao, W.: Finite element approximations for Stokes-Darcy flow with Beavers-Joseph interface conditions. SIAM J. Numer. Anal. **47**, 4239–4256 (2010)
5. Chen, W., Chen, P., Gunzburger, M., Yan, N.: Superconvergence analysis of FEMs for the Stokes-Darcy system. Math. Methods Appl. Sci. **33**, 1605–1617 (2010)
6. D'Angelo, C., Zunino, P.: Numerical approximation with Nitsches coupling of transient Stokes/Darcy's flow problems applied to hemodynamics. Appl. Numer. Math. **62**, 378–395 (2012)
7. Camano, J., Gatica, G.N., Oyarza, R., Ruiz-Baier, R., Venegas, P.: New fully-mixed finite element methods for the Stokes-Darcy coupling. Comput. Methods Appl. Mech. Eng. **295**, 362–395 (2015)
8. Rui, H., Zhang, R.: A unified stabilized mixed finite element method for coupling Stokes and Darcy flows. Comput. Methods Appl. Mech. Eng. **198**, 2692–2699 (2009)
9. Pacquaut, G., Bruchon, J., Moulin, N., Drapier, S.: Combining a level-set method and a mixed stabilized P1/P1 formulation for coupling Stokes-Darcy flows. Int. J. Numer. Methods Fluids **69**, 459–480 (2012)

10. Rivire, B., Yotov, I.: Locally conservative coupling of Stokes and Darcy flows. SIAM J. Numer. Anal. **42**, 1959–1977 (2005)
11. Rivire, B.: Analysis of a discontinuous finite element method for the coupled Stokes and Darcy problems. J. Sci. Comput. **22**, 479–500 (2005)
12. Girault, V., Rivire, B.: DG Approximation of coupled Navier-Stokes and Darcy Equations by Beaver-Joseph-Saffman interface condition. SIAM J. Numer. Anal. **47**, 2052–2089 (2009)
13. Kanschat, G., Rivire, B.: A strongly conservative finite element method for the coupling of Stokes and Darcy flow. J. Comput. Phys. **229**, 5933–5943 (2010)
14. Lipnikov, K., Vassilev, D., Yotov, I.: Discontinuous Galerkin and mimetic finite difference methods for coupled Stokes-Darcy flows on polygonal and polyhedral grids. Numer. Math. **126**, 321–360 (2014)
15. Arbogast, T., Gomez, M.S.M.: A discretization and multigrid solver for a Darcy-Stokes system of three dimensional vuggy porous media. Comput. Geosci. **13**, 331–348 (2009)
16. Discacciati, M., Miglio, E., Quarteroni, A.: Mathematical and numerical models for coupling surface and groundwater flows. Appl. Numer. Math. **43**, 57–74 (2002)
17. Cai, M., Mu, M., Xu, J.: Preconditioning techniques for a mixed Stokes/Darcy model in porous media applications. J. Comput. Appl. Math. **233**, 346–355 (2009)
18. Girault, V., Vassilev, D., Yotov, I.: Mortar multiscale finite element methods for Stokes-Darcy flows. Numer. Math. **127**, 93–165 (2014)
19. Vassilev, D., Wang, C., Yotov, I.: Domain decomposition for coupled Stokes and Darcy flows. Comput. Methods Appl. Mech. Eng. **268**, 264–283 (2014)
20. Cao, Y., Gunzburger, M., He, X.-M., Wang, X.: Parallel, non-iterative, multi-physcis domain decomposition methods for time-dependent Stokes-Darcy systems. Math. Comput. **83**, 1617–1644 (2014)
21. He, X.-M., Li, J., Lin, Y., Ming, J.: A domain decomposition method for the steady-state Navier-Stokes-Darcy model with Beavers-Joseph interface condition. SIAM J. Sci. Comput. **37**, 264–290 (2015)
22. Layton, W., Schieweck, F., Yotov, I.: Coupling fluid flow with porous media flow. SIAM J. Numer. Anal. **40**, 2195–2218 (2002)
23. Gatica, G.N., Meddahi, S., Oyarza, R.: A conforming mixed finite-element method for the coupling of fluid flow with porous media flow. IMA J. Numer. Anal. **29**, 86–108 (2009)
24. Babuka, I., Gatica, G.N.: A residual-based a posteriori error estimator for the Stokes-Darcy coupled problem. SIAM J. Numer. Anal. **48**, 498–523 (2010)
25. Mu, M., Xu, J.: A two-grid method of a mixed Stokes-Darcy model for coupling fluid flow with porous media flow. SIAM J. Numer. Anal. **45**, 1801–1813 (2007)
26. Cai, M., Mu, M., Xu, J.: Numerical solution to a mixed Navier-Stokes/Darcy model by the two-grid approach. SIAM J. Numer. Anal. **47**, 3325–3338 (2009)
27. Mu, M., Zhu, X.: Decoupled schemes for a nonstationary mixed Stokes-Darcy model. Math. Comput. **79**, 707–731 (2010)
28. Shan, L., Zheng, H.: Partitioned time stepping method for fully evolutionary Stokes-Darcy flow with Beavers-Joseph interface conditions. SIAM J. Numer. Anal. **51**, 813–839 (2013)
29. Tlupova, S., Cortez, R.: Boundary integral solutions of coupled Stokes and Darcy flows. J. Comput. Phys. **228**, 158–179 (2009)
30. Boubendir, Y., Tlupova, S.: Stokes-darcy boundary integral solutions using preconditioners. J. Comput. Phys. **228**, 8627–8641 (2009)
31. Wang, W., Xu, C.: Spectral methods based on new formulations for coupled Stokes and Darcy equations. J. Comput. Phys. **257**, 126–142 (2014)
32. Hessari, P.: Pseudospectral least squares method for Stokes-Darcy equations. SIAM J. Numer. Anal. **53**, 1195–1213 (2015)
33. Rybak, I., Magiera, J., Helmig, R., Rohde, C.: Multirate time integration for coupled saturated/unsaturated porous medium and free flow systems. Comput. Geosci. **19**, 299–309 (2015)
34. Li, Z.: An augmented Cartesian grid method for Stokes-Darcy fluid-structure interactions. Int. J. Numer. Methods Eng. **106**, 556–575 (2016)
35. Chen, J., Sun, S., Wang, X.: A numerical method for a model of two-phase flow in a coupled free flow and porous media system. J. Comput. Phys. **268**, 1–16 (2014)
36. Han, D., Sun, D., Wang, X.: Two-phase flows in karstic geometry. Math. Methods Appl. Sci. **37**, 3048–3063 (2014)
37. Han, D., Wang, X., Wu, H.: Existence and uniqueness of global weak solutions to a Cahn-Hilliard-Stokes-Darcy system for two phase incompressible flows in karstic geometry. Journal of Differential Equations **257**, 3887–3933 (2014)
38. Diegel, A.E., Feng, X., Wise, S.M.: Analysis of a mixed finite element method for a Cahn-Hilliard-Darcy-Stokes system. SIAM J. Numer. Anal. **53**, 127–152 (2015)
39. Chen, W., Han, D., Wang, X.: Uniquely solvable and energy stable decoupled numerical schemes for the Cahn-Hilliard-Stokes-Darcy system for two-phase flows in karstic geometry. Numer. Math. **137**, 229–255 (2017)
40. Gao, Y., He, X., Mei, L., Yang, X.: Decoupled, linear, and energy stable finite element method for the Cahn-Hilliard-Navier-Stokes-Darcy phase field model. SIAM J. Sci. Comput. **40**, B110–B137 (2018)
41. Bukuca, M., Yotov, I., Zakerzadeh, R., Zunino, P.: Partitioning strategies for the interaction of a fluid with a poroelastic material based on a nitsches coupling approach. Comput. Methods Appl. Mech. Eng. **292**, 138–170 (2015)
42. Hou, J., Qiu, M., He, X., Guo, C., Wei, M., Bai, B.: A dual-porosity-Stokes model and finite element method for coupling dual-porosity flow and free flow. SIAM J. Sci. Comput. **38**, B710–B739 (2016)
43. Chen, W., Gunzburger, M., Sun, D., Wang, X.: Efficient and long-time accurate second-order methods for the Stokes-Darcy system. SIAM J. Numer. Anal. **51**, 2563–2584 (2013)
44. Discacciati, M., Oyarza, R.: A conforming mixed finite element method for the Navier-Stokes/Darcy coupled problem. Numer. Math. **135**, 571–606 (2017)
45. Badea, L., Discacciati, M., Quarteroni, A.: Numerical analysis of the Navier-Stokes/Darcy coupling. Numer. Math. **115**, 195–227 (2010)
46. Jacimovic, N., Hosoda, T., Kishida, K., Ivetic, M.: Numerical solution of the Navier-Stokes equations for incompressible flow in porous media with free surface boundary. J. Appl. Mech. **8**, 225–231 (2005)
47. Cesmelioglu, A., Rivire, B.: Analysis of time-dependent Navier-Stokes flow coupled with Darcy flow. J. Numer. Math. **16**, 249–280 (2008)
48. Chorin, A.J.: Numerical solution of the Navier-Stokes equations. Math. Comput. **22**, 745–762 (1968)
49. Shiue, M.-C., Ong, K.C., Lai, M.-C.: Convergence of the MAC scheme for the Stokes/Darcy coupling problem. J. Sci. Comput. **76**, 1216–1251 (2018)
50. Beavers, G., Joseph, D.: Boundary conditions at a naturally impermeable wall. J. Fluid Mech. **30**, 197–207 (1967)
51. Saffman, P.: On the boundary conditions at the interface of a porous media. Stud. Appl. Math. **50**, 93–101 (1971)
52. Patankar, S.V.: Numerical Heat Transfer and Fluid Flow. Hemisphere Publishing Corporation, New York (1980)
53. Fletcher, C.A.J.: Computational Techniques for Fluid Dynamics. Springer, Berlin (1991)